Chapter 7
Multicomponent DNLS Equations

One of the most interesting extensions of the DNLS equation is in the study of multicomponent versions of the model. Such models are relevant both in nonlinear optics, e.g., when propagating multiple frequencies or polarizations of light; prototypical examples of these types have been discussed, e.g., in [1, 2] from the theoretical point of view and in [3] from the experimental point of view (see also references therein). On the other hand, similar models are quite relevant to two-component [4] or even one-component BECs [5] in the presence of optical lattice potentials. The coupling between the different components can be linear or nonlinear (or both) [1]. In this chapter, we show some case examples of interesting dynamics that can arise in the linear coupling case (symmetry breaking), as well as ones that can arise in the nonlinear coupling case (dynamical instabilities).

7.1 Linearly Coupled

In the context of optics, systems of linearly coupled DNLS equations are relevant to various applications: linear coupling may occur among two polarization modes inside each waveguide of a waveguide array, being induced by a twist of the core (for linear polarizations), or by the birefringence (for circular polarizations). Linear coupling between two modes also takes place in arrays of dual-core waveguides [1]. On the other hand, in BECs, the linear coupling may be imposed by an external microwave or radio frequency field, which can drive Rabi [6, 7] or Josephson [8, 9] oscillations between populations of two different states.

In both optical and atomic media, the basic linearly coupled DNLS model takes the following form:

$$\begin{cases} iU_t = K\epsilon\Delta_2 U + KV + |U|^2 U, \\ iV_t = K\epsilon\Delta_2 V + KU + |V|^2 V, \end{cases} \tag{7.1}$$

where $U = U(\boldsymbol{x}, t)$ and $V = V(\boldsymbol{x}, t)$ are wave functions of the two species in BEC, or electric field envelopes of the two coupled modes in optics ($\boldsymbol{x}$ is realized

P.G. Kevrekidis, *The Discrete Nonlinear Schrödinger Equation*, STMP 232, 153–171, DOI 10.1007/978-3-540-89199-4_7, © Springer-Verlag Berlin Heidelberg 2009

as a discrete vectorial coordinate), K is the strength of the linear coupling between fields U and V, and ϵ determines the couplings between adjacent sites of the lattice. For convenience, the full lattice-coupling constant is defined as $K\epsilon$ (this will allow us to scale out K from the analysis presented below).

Following the analysis of [10], we seek stationary solutions to the equations in the form

$$\begin{cases} U(\boldsymbol{x}, t) = \sqrt{K}\, u(\boldsymbol{x}) \exp[-iK(\mu - 2D\epsilon)t], \\ V(\boldsymbol{x}, t) = \sqrt{K}\, v(\boldsymbol{x}) \exp[-iK(\mu - 2D\epsilon)t], \end{cases} \tag{7.2}$$

where $u(\boldsymbol{x})$ and $v(\boldsymbol{x})$ are real-valued functions, and μ is an appropriately shifted chemical potential. Then the steady-state equations become

$$\begin{cases} \mu u_n = \epsilon \overline{\Delta}_1 u_n + v_n + u_n^3, \\ \mu v_n = \epsilon \overline{\Delta}_1 v_n + u_n + v_n^3, \end{cases} \tag{7.3}$$

with $\overline{\Delta}_1 w_n \equiv w_{n+1} + w_{n-1}$. In the two-dimensional case, the stationary equations are

$$\begin{cases} \mu u_{n,m} = \epsilon \overline{\Delta}_2 u_{n,m} + v_{n,m} + u_{n,m}^3, \\ \mu v_{n,m} = \epsilon \overline{\Delta}_2 v_{n,m} + u_{n,m} + v_{n,m}^3, \end{cases} \tag{7.4}$$

where $\overline{\Delta}_2 w_{n,m} \equiv w_{n+1,m} + w_{n-1,m} + w_{n,m+1} + w_{n,m-1}$.

In [10], both symmetric (with $u = v$) and symmetry-broken (with $u \neq v$) states were constructed as solutions of Eqs. (7.3) and (7.4). Since we are interested here in the properties of the fundamental single-site states, we will use as a reasonably accurate method to obtain an analytical handle on the waveforms the variational approximation (comparing it with the full numerical results). We start by noting that Eqs. (7.3) and (7.4) can be derived from the following Lagrangians:

$$L_{1\mathrm{D}} = \sum_{n=-\infty}^{\infty} \left[-\frac{\mu}{2}\left(u_n^2 + v_n^2\right) + \frac{1}{4}\left(u_n^4 + v_n^4\right) + u_n v_n + \epsilon\left(u_{n+1}u_n + v_{n+1}v_n\right) \right], \tag{7.5}$$

$$\begin{aligned} L_{2\mathrm{D}} = \sum_{m,n=-\infty}^{\infty} \Bigg[& -\frac{\mu}{2}\left(u_{n,m}^2 + v_{n,m}^2\right) + \frac{1}{4}\left(u_{n,m}^4 + v_{n,m}^4\right) + u_{n,m}v_{n,m} \\ & + \epsilon(u_{n+1,m}u_{n,m} + u_{n,m+1}u_{n,m} + v_{n+1,m}v_{n,m} + v_{n,m+1}v_{n,m}) \Bigg]. \end{aligned} \tag{7.6}$$

Then, the discrete soliton *ansätze*, $\{u_n, v_n\} = \{A, B\}e^{-\lambda|n|}$ and $\{u_{n,m}, v_{n,m}\} = \{A, B\}e^{-\lambda|n|}e^{-\lambda|m|}$, with free constants A, B, and $\lambda > 0$, are used in the one- and two-dimensional cases, respectively, as in our earlier analysis in Chaps. 2 and 3. It should be noted in comparison to the standard one-component ansatz that by introducing different amplitudes A and B, we admit a possibility of *asymmetric solitons*, within the framework of the variational approximation.

The resulting expressions for the effective Lagrangians are

$$\begin{aligned}
L_{1\mathrm{D}} &= \left[AB - \frac{\mu}{2}\left(A^2+B^2\right)\right]\coth\lambda + \frac{1}{4}\left(A^4+B^4\right)\coth(2\lambda) \\
&\quad +\epsilon\left(A^2+B^2\right)\mathrm{cosech}\lambda, \\
L_{2\mathrm{D}} &= \left[AB - \frac{\mu}{2}\left(A^2+B^2\right)\right]\coth^2\lambda + \frac{1}{4}\left(A^4+B^4\right)\coth^2 2\lambda \\
&\quad +2\epsilon\left(A^2+B^2\right)(\mathrm{cosech}\lambda)\coth\lambda.
\end{aligned}$$

Then, deriving the static version of the Euler–Lagrange equations $\partial L_{1\mathrm{D},2\mathrm{D}}/\partial(\lambda, A, B) = 0$ yields

$$\begin{gathered}
\frac{\mu}{2}\left(A^2+B^2\right)\mathrm{cosech}^2\lambda - \frac{1}{2}\left(A^4+B^4\right)\mathrm{cosech}^2 2\lambda \\
-AB\,\mathrm{cosech}^2\lambda - \epsilon\left(A^2+B^2\right)\mathrm{cosech}\lambda\coth\lambda = 0, \\
-\mu A\coth\lambda + A^3\coth 2\lambda + B\coth\lambda + 2\epsilon A\,\mathrm{cosech}\lambda = 0, \\
-\mu B\coth\lambda + B^3\coth 2\lambda + A\coth\lambda + 2\epsilon B\,\mathrm{cosech}\lambda = 0
\end{gathered}$$

for the one-dimensional case, and

$$\begin{gathered}
\mu\left(A^2+B^2\right)\coth\lambda\,\mathrm{cosech}^2\lambda - \left(A^4+B^4\right)\coth 2\lambda\,\mathrm{cosech}^2 2\lambda \\
-2AB\coth\lambda\,\mathrm{cosech}^2\lambda - 2\epsilon\left(A^2+B^2\right)\left(\mathrm{cosech}\lambda\coth^2\lambda + \mathrm{cosech}^3\lambda\right) = 0, \\
-\mu A\coth^2\lambda + A^3\coth^2 2\lambda + B\coth^2\lambda + 4\epsilon A\,\mathrm{cosech}\lambda\coth\lambda = 0, \\
-\mu B\coth^2\lambda + B^3\coth^2 2\lambda + A\coth^2\lambda + 4\epsilon B\,\mathrm{cosech}\lambda\coth\lambda = 0
\end{gathered}$$

for the two-dimensional fundamental waves.

An interesting observation consists of the analytically tractable AC limit of $\epsilon = 0$. For the symmetric branch, we then have $u_n = v_n = 0$ or $u_n = v_n = \sqrt{\mu - 1}$, while for the asymmetric branch, a system of algebraic equations has to be solved $\mu u_n = v_n + u_n^3$, $\mu + 1 = u_n^2 + u_n v_n + v_n^2$. The solution is shown in Fig. 7.1, which displays the symmetry-breaking bifurcation in the AC limit, by means of a plot of the *asymmetry measure*, $r \equiv (E_1 - E_2)/(E_1 + E_2)$, versus half the total norm, $E = (E_1 + E_2)/2$, where $\{E_1, E_2\} = \sum_n \left\{u_n^2, v_n^2\right\}$ are the norms of the two components of the solution. It is particularly interesting to point out that in the case of $\epsilon = 0$, the observed pitchfork bifurcation is *supercritical* (cf. with the finite ϵ case below).

Fig. 7.1 From [10]: the bifurcation diagram for the discrete solitons in the anti-continuum limit, $\epsilon = 0$; r and E are the asymmetry parameter and the half of the total squared norm, respectively. The *solid* and *dashed* lines represent stable and unstable solutions, respectively

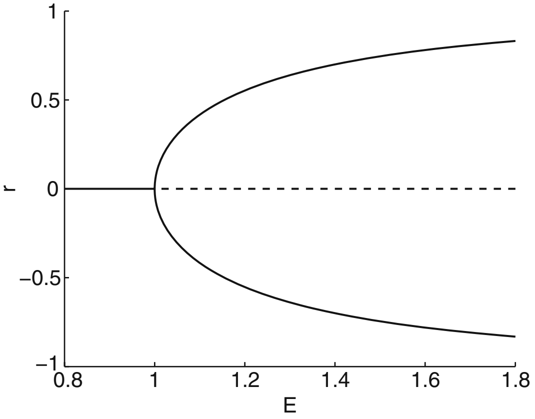

These results can be compared with those of direct numerical continuation of the corresponding branches from the AC limit. In [10] the relevant branches were obtained and their numerical linear stability was also examined using the perturbed solution ansatz

$$\begin{cases} U(\boldsymbol{x},t) = e^{-i\mu t}\left[u(\boldsymbol{x}) + a(\boldsymbol{x})\,e^{\lambda t} + b^*(\boldsymbol{x})\,e^{\lambda^* t}\right], \\ V(\boldsymbol{x},t) = e^{-i\mu t}\left[v(\boldsymbol{x}) + c(\boldsymbol{x})\,e^{\lambda t} + d^*(\boldsymbol{x})\,e^{\lambda^* t}\right] \end{cases} \tag{7.7}$$

in Eqs. (7.1) and solving the resulting linearized equations for the perturbation eigenmodes a, b, c, d and the eigenvalues λ associated with them.

Typical results for particular values of ϵ are shown in Figs. 7.2 and 7.3, for the one- and two-dimensional cases, respectively. In both cases, it is remarkable to observe that the relevant bifurcation is observed to be *subcritical* (instead of supercritical as in the AC limit) pitchfork due to the collision of the fundamental

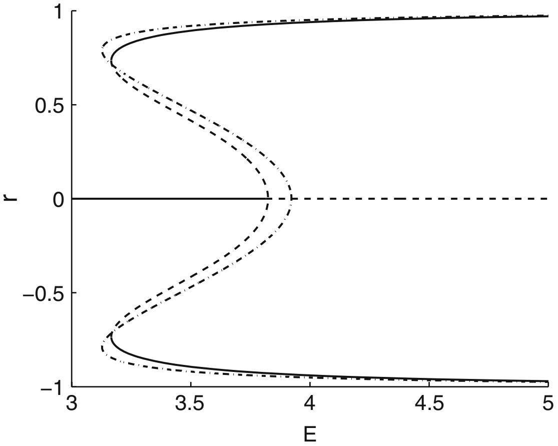

Fig. 7.2 From [10]: the bifurcation diagram is shown for $\epsilon = 1.6$ in the one-dimensional model. The *dash–dotted line* indicates solutions found through the variational approximation, while *solid* and *dashed lines* show, respectively, numerically found stable and unstable steady-state solutions

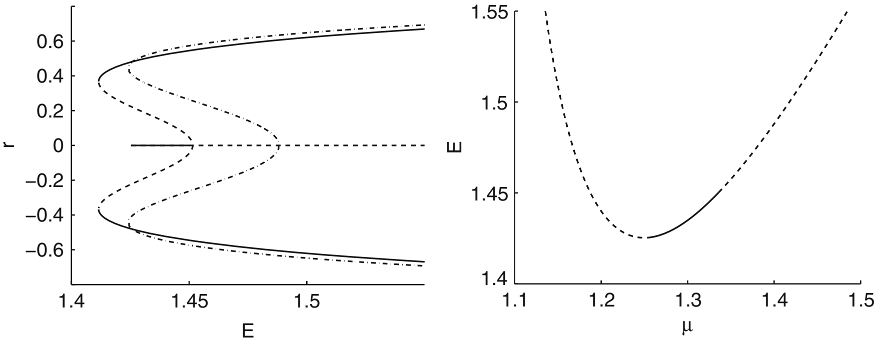

Fig. 7.3 From [10]: the *left panel* shows the bifurcation diagram in the two-dimensional model for $\epsilon = 0.25$, in the same way (i.e., with the same meaning of the different curves) as the one-dimensional diagram is shown in Fig. 7.2. The *right panel* displays the dependence of the solution's squared norm, E, upon the chemical potential, μ, for the symmetric solutions. Unlike the one-dimensional case, there are now two different symmetric solutions, resulting in both stable (*solid line*) and unstable (*dashed lines*) solutions for norms below the value at which the symmetric and asymmetric solution branches intersect

symmetric branch with two unstable asymmetric branches. The latter ones emerge through a saddle node bifurcation also generating a stable asymmetric branch. Interestingly, between the two critical points, both the symmetric branch and the outer asymmetric one are stable, hence there exists a region of bistability. We also observe that, in these typical comparisons, the results obtained from the variational approximation are quite close to the fully numerical results. This is more so in the one-dimensional case than in the two-dimensional case, since, as we have seen before (e.g., in Chap. 3), since the inaccuracy of the variational ansatz tends to accumulate the error in higher dimensions.

Typical examples of the existence and stability results obtained numerically, and how the former compare with the variational predictions are shown in Fig. 7.4 for the one-dimensional case and in Figs. 7.5 and 7.6 for the two-dimensional case. We note that in general the VA provides a fairly accurate description of the profile, although in some cases, it may yield slower decay rates (and slightly different amplitudes) than the full numerical results. It should also be reminded to the reader that in the two-dimensional case, as discussed in Chap. 3, there are typically two (symmetric) solutions corresponding to the same norm, namely a stable and an unstable one, as is shown, e.g., in Fig. 7.6 (see also the right panel of Fig. 7.3).

There are a couple of physically relevant observations to be made here. On the one hand, a conclusion following from the comparison of Figs. 7.1 and 7.2 is that the bifurcation found in the AC limit (see Fig. 7.1) is supercritical, unlike the weakly subcritical one in Fig. 7.2. This indicates that the character of the pitchfork bifurcation should change from subcritical to supercritical with the increase of discreteness, i.e., decrease of ϵ, which, in turn, should eliminate the unstable asymmetric branches. In accordance with this expectation, it was found in [10] that the unstable asymmetric solutions exist only for $\epsilon > 0.35$, in the one-dimensional case.

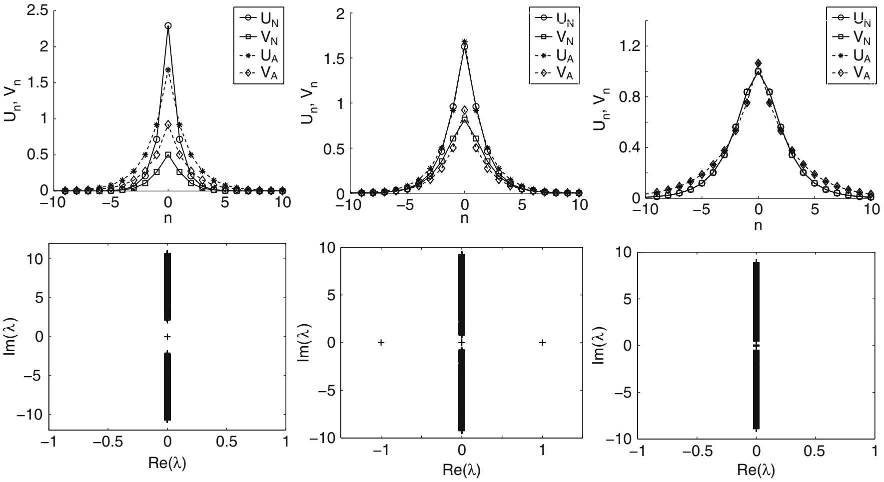

Fig. 7.4 From [10]: plots of solutions belonging to different branches in Fig. 7.2, at $E = 3.4$. The *top row* figures show the solution profiles found by means of the numerical (U_N, V_N) and variational ("analytical", U_A, V_A) methods. The *bottom row* plots illustrate the linear stability eigenvalues for the numerical solution. The *first column* presents a stable stationary asymmetric solution belonging to the outer (upper) branch in Fig. 7.2, the *second column* is an unstable asymmetric solution, and the last column shows a stable solution of the symmetric family

On the other hand, in the two-dimensional case, the bifurcation diagram has no continuum analog due to the occurrence of collapse, contrary to what is the case in one-dimension. In the two-dimensional case also, due to the existence of a minimum norm threshold below which the symmetric branch does not exist, as discussed in Chap. 3 [11–14], it is possible that the asymmetric solution (as in Fig. 7.3) will exist for powers below the symmetric solution's excitation threshold. This will enable the system to access lower norm states than in its one-component incarnation. Finally, it should be pointed out that the bistability arising from Figs. 7.2 and 7.3 above has been used in [10] to successfully "steer" the unstable asymmetric solitons dynamically toward either the stable symmetric or the stable asymmetric branch, depending on the type of the original "kick" (i.e., perturbation) to the unstable solution.

7.2 Nonlinearly Coupled

In the context of nonlinearly coupled DNLS equations, numerous studies have been present at the theoretical level discussing the properties of solitary waves, both in one dimension [15–17], and in two-dimensions [1, 15, 18–20], as well as even in three dimensions [21]. However, experimental results in this system materialized, to the best of our knowledge, only very recently in [3] (see also the longer exposition of [22]). These experimental realizations resulted in further theoretical work addressing various aspects of nonlinearly coupled multicomponent models including

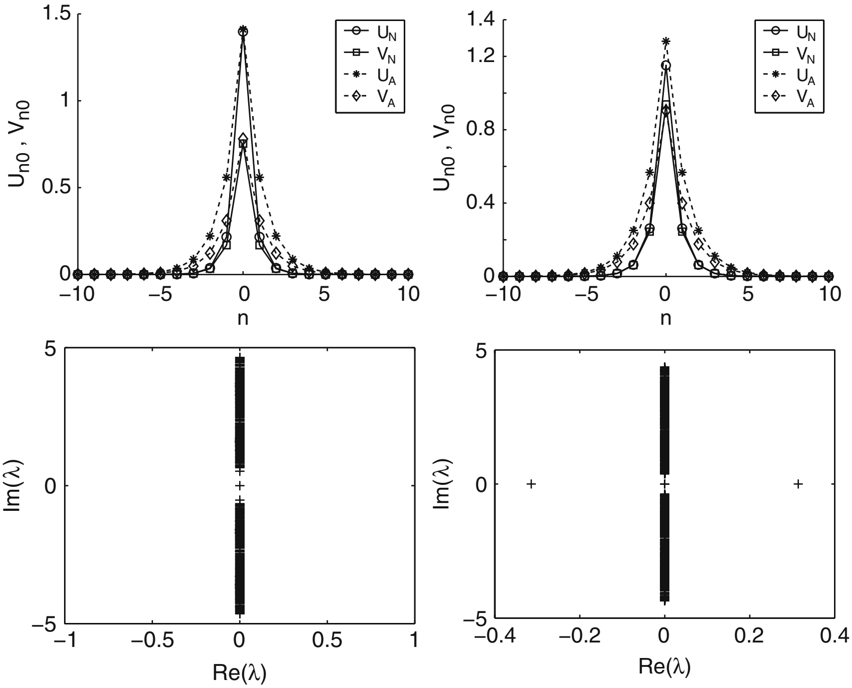

Fig. 7.5 From [10]: cross section plots of the asymmetric solutions belonging to different branches in Fig. 7.3, at $E = 1.435$. The *top row* figures show the solutions found by means of the numerical (U_N, V_N) and variational ("analytical," U_A, V_A) methods, and the *bottom row* plots display linear stability eigenvalues for the numerical solution. The *first* and *second* columns represent, respectively, stable and unstable solutions belonging to the asymmetric branches of the bifurcation diagram, respectively

switching and instability-induced amplification, modulational instability, PN barriers, and stability of localized modes among others [2, 23–25]. Here, we restrict ourselves to the study of the fundamental modes of the system in one dimension and a small sampler of the interesting possibilities that arise in higher dimensions (including multivortex structures, etc.). We refer the interested reader to the above literature for further details.

7.2.1 One Dimension

The theoretical model put forth in [3] to analyze the experimental results was of the form

$$i\dot{a}_n = -a_n - \epsilon\left(a_{n+1} + a_{n-1}\right) - \left(|a_n|^2 + A|b_n|^2\right)a_n - Bb_n^2 a_n^{\star}, \tag{7.8}$$

$$i\dot{b}_n = b_n - \epsilon\left(b_{n+1} + b_{n-1}\right) - \left(|b_n|^2 + A|a_n|^2\right)b_n - Ba_n^2 b_n^{\star}. \tag{7.9}$$

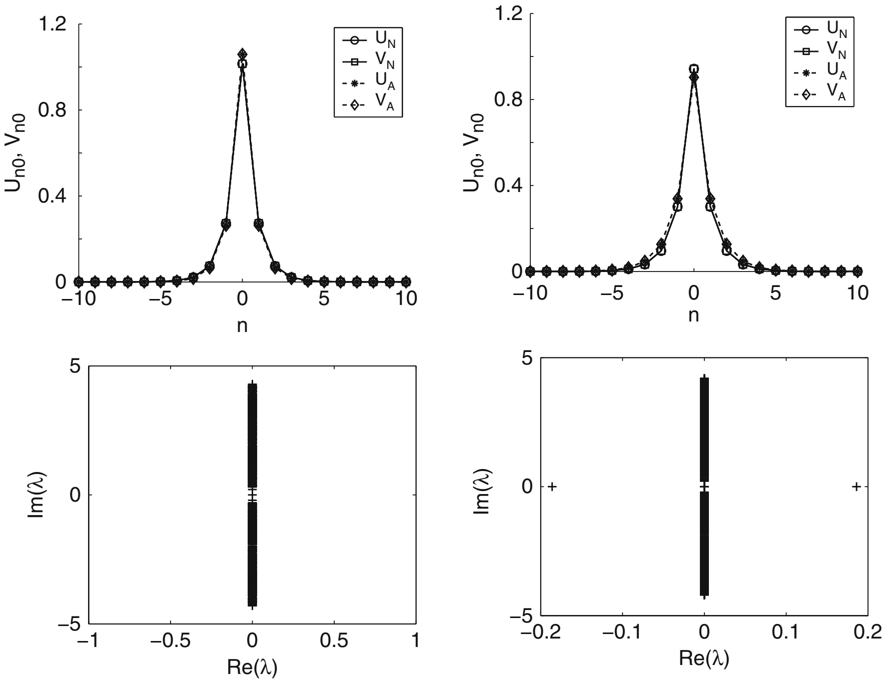

Fig. 7.6 Same as Fig. 7.5 for two symmetric solutions found at $E = 1.435$

In the experimental context, a_n and b_n are the appropriately normalized, slowly varying, complex field envelopes for the transverse electric (TE) and transverse magnetic (TM) polarized waves, respectively. The constants A and B are respectively associated with the cross-phase modulation (XPM) and four-wave mixing (FWM) and were evaluated in the experiments of [3] to be approximately equal to $A \simeq 1$ and $B \simeq 1/2$. It is interesting to note that in this case, due to the FWM term, only the total power (instead of the individual powers of each component, as would be the case if $B = 0$)

$$P = \sum_n \left(|a_n|^2 + |b_n|^2\right) \tag{7.10}$$

is conserved and based on the analysis of [3], it is connected to the dimensional power P_d (measured in watts) through $P_d \simeq 56.4P$. While in the analysis of [2], which we will follow here, the dimensionless coupling ϵ was considered a free parameter, in the experimental results reported in [3], it was $\epsilon \approx 0.921$.

Seeking stationary solutions in the form $a_n = \tilde{a}_n e^{iqz}$ and $b_n = \tilde{b}_n e^{iqz}$ and subsequently dropping the tildes, results in the following stationary equations:

$$(q-1)a_n - \epsilon\,(a_{n+1}+a_{n-1}) - \left(|a_n|^2 + A|b_n|^2\right)a_n - Bb_n^2 a_n^\star = 0, \tag{7.11}$$

$$(q+1)b_n - \epsilon\,(b_{n+1}+b_{n-1}) - \left(|b_n|^2 + A|a_n|^2\right)b_n - Ba_n^2 b_n^\star = 0. \tag{7.12}$$

The dimensionless propagation constant q is then an additional (to the dimensionless coupling ϵ) free parameter and it is in the (ϵ, q) two-parameter plane that the results presented herein are given.

The linear stability of a given stationary solution (a_n^0, b_n^0) of the stationary equations (7.11) and (7.12) can be obtained through the usual perturbation ansatz

$$a_n = a_n^0 + \delta\left(c_n e^{-i\omega z} + d_n e^{i\omega^\star z}\right), \tag{7.13}$$

$$b_n = b_n^0 + \delta\left(f_n e^{-i\omega z} + g_n e^{i\omega^\star z}\right). \tag{7.14}$$

Then the matrix eigenvalue problem yielding the eigenfrequency ω reads

$$\omega \begin{pmatrix} c_n \\ d_n^\star \\ f_n \\ g_n^\star \end{pmatrix} = \mathbf{L}\cdot \begin{pmatrix} c_n \\ d_n^\star \\ f_n \\ g_n^\star \end{pmatrix},$$

where

$$\mathbf{L} = \begin{pmatrix} L_{11} & L_{12} & L_{13} & L_{14} \\ L_{21} & L_{22} & L_{23} & L_{24} \\ L_{31} & L_{32} & L_{33} & L_{34} \\ L_{41} & L_{42} & L_{43} & L_{44} \end{pmatrix}.$$

The $N \times N$ (where N is the size of the lattice) blocks of the linearization matrix are given by

$$L_{11} = (q-1) - \epsilon\,(\Delta_2 + 2) - 2\left|a_n^0\right|^2 - A\left|b_n^0\right|^2, \tag{7.15}$$

$$L_{12} = -\left(a_n^0\right)^2 - B\left(b_n^0\right)^2, \tag{7.16}$$

$$L_{13} = -Aa_n^0\left(b_n^0\right)^\star - 2B\left(a_n^0\right)^\star b_n^0, \tag{7.17}$$

$$L_{14} = -Aa_n^0 b_n^0, \tag{7.18}$$

$$L_{21} = -L_{12}^\star, \tag{7.19}$$

$$L_{22} = -L_{11}, \tag{7.20}$$

$$L_{23} = -L_{14}^\star, \tag{7.21}$$

$$L_{24} = -L_{13}^\star, \tag{7.22}$$

$$L_{31} = L_{13}^{\star}, \tag{7.23}$$

$$L_{32} = L_{14}, \tag{7.24}$$

$$L_{33} = (q+1) - \epsilon\,(\Delta_2 + 2) - 2\left|b_n^0\right|^2 - A\left|a_n^0\right|^2, \tag{7.25}$$

$$L_{34} = -\left(b_n^0\right)^2 - B\left(a_n^0\right)^2, \tag{7.26}$$

$$L_{41} = -L_{14}^{\star}, \tag{7.27}$$

$$L_{42} = -L_{13}, \tag{7.28}$$

$$L_{43} = -L_{34}^{\star}, \tag{7.29}$$

$$L_{44} = -L_{33}. \tag{7.30}$$

In the above, we use the shorthand notation $(\Delta_2 + 2)z_n = z_{n+1} + z_{n-1}$. In [2], this eigenvalue problem was solved fully in the AC limit of $\epsilon = 0$ for the fundamental branches and subsequent numerical continuation was used to determine the stability of the branches for finite values of ϵ.

We first examine the AC limit of individual sites whose complex fields we decompose as $a_n = r_n e^{i\theta_n}$ and $b_n = s_n e^{i\phi_n}$, obtaining from Eqs. (7.11) and (7.12)

$$(q-1) - \left(r_n^2 + A s_n^2\right) - B s_n^2 e^{2i(\phi_n - \theta_n)} = 0, \tag{7.31}$$

$$(q+1) - \left(s_n^2 + A r_n^2\right) - B r_n^2 e^{-2i(\phi_n - \theta_n)} = 0. \tag{7.32}$$

From these equations, we obtain

$$\theta_n - \phi_n = k\frac{\pi}{2} \tag{7.33}$$

with $k \in \mathcal{Z}$. The simplest possible solutions are the ones that involve only one of the two branches and were hence termed TE and TM modes, respectively, in [26]. The TE solution of Eqs. (7.31) and (7.32) has the form (in the present limit)

$$r_n = \pm\sqrt{q-1}, \quad s_n = 0 \tag{7.34}$$

and exists only for $q > 1$. On the other hand, the TM mode features

$$r_n = 0, \quad s_n = \pm\sqrt{q+1} \tag{7.35}$$

and is only present for $q > -1$.

In addition to these, there are two possible mixed mode solutions allowed by Eq. (7.33). The first one ($e^{2i(\theta_n - \phi_n)} = 1$) was characterized as a linearly polarized (LP) branch in [3], involving in-phase contributions from both the TE and TM components. In this case, the linear system of Eqs. (7.31) and (7.32) has the general solution

$$r_n = \pm\sqrt{\frac{(A+B)(q+1)-(q-1)}{(A+B)^2-1}}, \tag{7.36}$$

$$s_n = \pm\sqrt{\frac{(A+B)(q-1)-(q+1)}{(A+B)^2-1}}. \tag{7.37}$$

If $(A+B)^2 > 1$ (as was the case in the experiment of [3]), this branch only exists for $(A+B)(q+1) > (q-1)$ and $(A+B)(q-1) > (q+1)$ (the sign of the two above inequalities should be reversed for existence conditions in the case of $(A+B)^2 < 1$). Among the two conditions, in the present setting, the second one is the most "stringent" for the case $A = 2B = 1$, which yields the constraint $q \geq 5$ (while the first condition requires for the same parameters $q \geq -5$). Finally, the second mixed mode possibility with $e^{2i(\theta_n-\phi_n)} = -1$ represents the so-called elliptically polarized mode (EP) with amplitudes

$$r_n = \pm\sqrt{\frac{(A-B)(q+1)-(q-1)}{(A-B)^2-1}}, \tag{7.38}$$

$$s_n = \pm\sqrt{\frac{(A-B)(q-1)-(q+1)}{(A-B)^2-1}}. \tag{7.39}$$

If $(A-B)^2 < 1$ (as is experimentally the case), the EP branch will exist if $q-1 \geq (A-B)(q+1)$ and $q+1 \geq (A-B)(q-1)$ (once again the signs should be reversed if $(A-B)^2 > 1$). Here, the first condition is more constraining than the second, imposing for $A = 2B = 1$ that $q \geq 3$ (while the second condition only requires $q \geq -3$).

We now turn to the analysis of the stability of the various single-site branches (TE, TM, LP, and EP) that can be constructed at the AC limit with one excited site, while all others are inert. It is straightforward to see [2] from direct inspection of the stability matrix that the inert sites yield a pair of eigenfrequencies at $\pm(q-1)$, as well as one at $\pm(q+1)$. On the other hand, the excited site will yield a non-trivial 4×4 block in the stability matrix. One pair of the eigenvalues of that block will be at $\omega = 0$ due to the gauge invariance of the solution, associated with the conservation of the total power P. The other pair in the case of the TE mode will be

$$\omega_{TE} = \pm\sqrt{(q+1)^2 + (A^2-B^2)(q-1)^2 - 2A(q^2-1)}. \tag{7.40}$$

Examining our model for the experimental case of $A = 1$, $B = 1/2$, and $q > 0$, we find that this eigenfrequency is real for $q < 5$, while it is imaginary for $q > 5$ (hence implying the presence of an instability, due to the corresponding eigenvalue $\lambda = i\omega$ becoming real). The mode is stable, on the other hand, for $1 < q < 5$. Similar considerations for the TM mode yield

$$\omega_{TM} = \pm\sqrt{(q-1)^2 + (A^2 - B^2)(q+1)^2 - 2A(q^2-1)}, \tag{7.41}$$

leading to stability for $-1 < q < 3$, and instability for $q > 3$. Finally, for the LP and EP modes, following [2], we only give the results for $A \approx 2B \approx 1$ as

$$\omega_{LP} = \pm\frac{2\sqrt{2}}{5}\sqrt{q^2-25} \tag{7.42}$$

and

$$\omega_{EP} \pm \frac{2\sqrt{2}}{3}\sqrt{q^2-9}, \tag{7.43}$$

suggesting stability for $q \geq 5$ and $q \geq 3$, respectively.

Based on the above observations, one can reconstruct the full picture at the AC limit (and, to be specific, for $A \approx 2B \approx 1$, although it is possible to do for any value of A and of B). In particular, the TE branch exists for $q \geq 1$ and is stable for $1 \leq q \leq 5$. For $q > 5$, the branch is destabilized as a new branch emerges, namely the LP branch, through a pitchfork bifurcation; note that the TM component of this branch, per Eq. (7.37) is exactly zero at $q = 5$, hence it directly bifurcates from the TE branch. The two branches of this supercritical pitchfork correspond to the two signs of s_n in Eq. (7.37). The bifurcating branch "inherits" the stability of the TE branch for all larger values of q, while the latter branch remains unstable thereafter. Similarly, the TM branch exists for $q \geq -1$ and is stable in the interval $-1 \leq q \leq 3$. However, at $q = 3$, a new branch (in fact, a pair thereof) bifurcates with non-zero r_n, beyond the bifurcation point, as in Eq. (7.38). This is accompanied by the destabilization of the TM branch (due to a real eigenvalue) and the *apparent* stability of the ensuing EP branch for all values of $q > 3$.

In the presence of finite coupling, it is firstly important to determine the nature of the continuous spectrum, by using $a_n \sim e^{i(kn-\omega z)}$ and $b_n \sim e^{i(kn-\omega z)}$. The resulting dispersion relations then read

$$\omega = (q-1) - 2\epsilon\cos(k), \tag{7.44}$$

$$\omega = (q+1) - 2\epsilon\cos(k). \tag{7.45}$$

Hence the continuous spectrum extends through the frequency intervals $[q-1-2\epsilon, q-1+2\epsilon]$ and $[q+1-2\epsilon, q+1+2\epsilon]$ (and their opposites), which for $\epsilon = 0$ degenerate to the isolated points $q-1$ and $q+1$ (obtained previously). Also, importantly, for $q-1 < 2\epsilon$ (equivalently for $\epsilon > (q-1)/2$), the continuous spectrum branch will be crossing the origin, leading to the collision of the eigenvalues with their mirror symmetric opposites, that will, in turn, lead to instabilities. For this reason, we need *only* consider couplings in the interval $\epsilon \in [0, (q-1)/2]$. Using the above pieces of information and two-parameter numerical continuation

Fig. 7.7 TE branch from [2]: the panel shows the two parameter bifurcation diagram of the coupling ϵ as a function of q. All the relevant existence and stability regimes have been accordingly labeled

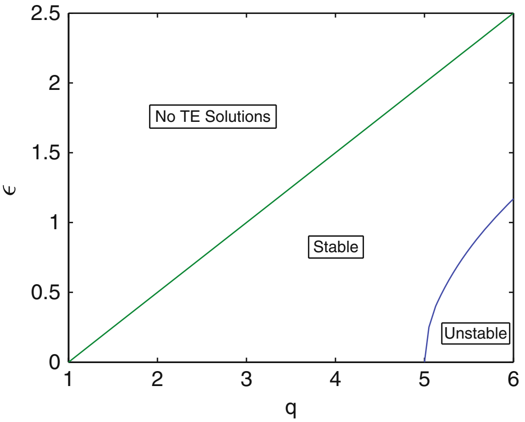

in [2], the numerical bifurcation diagrams of the different single-site branches were constructed, which we reproduce below.

The continuation of the TE branch is detailed in Fig. 7.7. For this branch, solutions cannot be obtained for $\epsilon > (q-1)/2$, i.e., the branch terminates at that point with its amplitude tending to zero at this point. Within its region of existence, the branch has a domain of stability and one of instability. The point of separation between the two in the AC limit, studied previously, was the critical point of $q = 5$. For $\epsilon \neq 0$, the separatrix curve is shown in Fig. 7.7 and can be well approximated numerically by the curve $\epsilon_{TE}^{c} \approx (4\sqrt{2}/5)\sqrt{q-5}$. Hence for $q \leq 5$, the solution is stable for all values of ϵ in its range of existence $(0 < \epsilon < (q-1)/2)$, while for $q \geq 5$, the solution is only stable for $\epsilon_{TE}^{c} < \epsilon < (q-1)/2$ and unstable (due to a real eigenvalue pair) for $0 < \epsilon < \epsilon_{TE}^{c}$.

The TM branch is somewhat more complicated than the TE one. Firstly, it does not disappear beyond the critical $\epsilon = (q-1)/2$; however, it does become unstable as predicted previously, hence we will, once again, restrict ourselves to this parameter range. Also, similarly to the TE branch case, there is an ϵ_{TM}^{c} below which the branch is *always* unstable, whereas for $\epsilon > \epsilon_{TM}^{c}$, the branch *may* be stable. At the AC limit, the critical point for the instability is $q = 3$, as discussed previously; for $q > 3$, the critical point is obtained numerically in Fig. 7.8. It can be well approximated numerically (close to $q = 3$) by $\epsilon_{TM}^{c} \approx (9/10)\sqrt{q-3}$.

However, within the range of *potential* stability ($0 \leq \epsilon \leq (q-1)/2$ for $q \leq 3$, and $\epsilon_{TM}^{c} \leq \epsilon \leq (q-1)/2$ for $q \geq 3$), we observe an additional large region of instability in the two-parameter bifurcation diagram of Fig. 7.8, due to a complex quartet of eigenvalues. This instability appears to stem from the point with $(q, \epsilon) = (2.2, 0)$ in the AC limit, and to linearly expand its range as ϵ increases. At $q = 2.2$ in the AC limit, the point spectrum eigenfrequency of Eq. (7.41) "collides" with the continuous spectrum point of concentration, corresponding to $\omega = q - 1$. However, this eigenvalue is associated with a negative Krein signature, i.e., opposite to that of the continuous band at $\omega = q - 1$ (see Chap. 2 for a detailed discussion of the Krein signature). The resulting collision therefore leads to the formation of a quartet

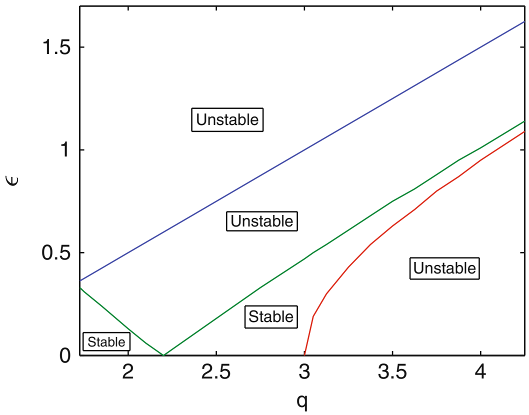

Fig. 7.8 Similarly to Fig. 7.7, the bifurcation diagram shows the two-parameter plane of stability of the TM branch

of eigenvalues emerging in the complex plane and, in turn, implying the instability of the TM configuration. As ϵ grows, the continuous spectrum band grows linearly in ϵ, hence the corresponding interval of q's, where this instability is present also grows at the same rate. Along the same vein, it is worth pointing out that the line of this instability threshold and that of $\epsilon = (q-1)/2$ are parallel.

The LP branch has in-phase contributions of the TE and TM modes and exists for $q > 5$. It emerges through a supercritical pitchfork as q is varied for fixed ϵ. Since this branch stems from the TE one, it only arises for $0 < \epsilon < \epsilon^c_{TE}$ and $q > 5$ and it is stable throughout its interval of existence, which is exactly the interval of Fig. 7.7 where the TE branch is found to be unstable.

Finally, the EP branch is shown in Fig. 7.9 and its description is somewhat analogous to that of the LP one. In particular, for fixed q close to (and larger than) 3 and varying ϵ, the branch exists and is *stable* for $0 < \epsilon < \epsilon^c_{TM}$, since it emerges from the TM branch through a supercritical pitchfork (as q is increased). Interestingly, for $q > 3.62$, this phenomenology appears to change and an expanding

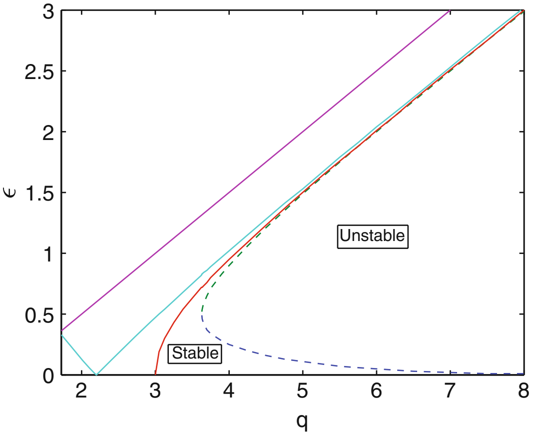

Fig. 7.9 The panel shows the two-parameter diagram for the EP mode from [2]. The region for $q > 3$ and $0 < \epsilon < \epsilon^c_{TM}$, where this modes exists is separated by the dashed line into a stable and an unstable regime. For comparison the extension of the regions of stability/instability of the TM mode from Fig. 7.8 are also included

(for increasing q) interval of oscillatory instability within the range of existence of the EP branch appears to arise. Returning to the AC limit, we note that the EP branch has a point spectrum eigenfrequency given by Eq. (7.43) with a negative Krein signature which upon collision with the continuous spectrum band of eigenfrequencies leads to instability. Setting the frequency of Eq. (7.43) equal to $q-1$, we obtain that this collision occurs at $q=9$. For lower values of q, this "collision" will occur for a finite (non-zero) interval of values of ϵ, which is the source of the oscillatory instability of the EP mode shown by the dashed line in Fig. 7.9.

7.2.2 *Higher Dimensions*

In addition to the one-dimensional incarnation of the above nonlinearly coupled mode, a number of studies have considered ground states [1] or excited states [19, 20] in two-dimensional DNLS lattices and even three-dimensional examples thereof [21]. Here we give some representative examples of these results and refer the interested reader to the corresponding references for more details.

In particular, in two-dimensional settings, among the most interesting solutions that it is possible to construct are the vortex pairs that were considered in [19]. Such pairs can have the form of the so-called double-charge configuration (S, S), where S is the topological charge of the structure, or the so-called hidden charge configuration $(S, -S)$, where the pair denotes the vorticity of each of the components. It was shown even in the continuum analog of NLS-type models that these distinct possibilities have *different* stability windows in terms of the model parameters [27, 28]. In particular, in the setting of [19], a so-called vortex cross configuration of charge $S=1$ was considered as the single-component building block consisting of a vortex on the four sites: $(-1,0)$, $(1,0)$, $(0,1)$, and $(0,-1)$. In fact, such a vortex cross inspired by a prototypical configuration of the form $u_{n,m} \propto \exp(i\phi) = \cos(\phi) + i\sin(\phi)$ was the original motivation in [29] for suggesting the existence of a discrete vortex in the context of the two-dimensional DNLS model. For this discrete vortex cross, the technique of the Lyapunov–Schmidt reductions as developed in Chap. 3 yields two pairs of imaginary eigenvalues $\lambda = \pm 2i\epsilon$, while a higher order calculation yields for the remaining pair of nonzero eigenvalues (since the fourth pair is at the origin due to the U(1) invariance) the approximation $\lambda = \pm 4i\epsilon^2$. The comparison of these predictions with the full numerical results is shown in Fig. 7.10, indicating good agreement with the analytical predictions for coupling strengths up to $\epsilon \approx 0.1$. The instability of this mode arises for $\epsilon \approx 0.395$.

Subsequently, the case of coupled vortices of the double charge and of the hidden charge variety were examined in the model

$$\left[i\frac{d}{dt} + C\Delta_2 + \begin{pmatrix} |\phi_{m,n}|^2 & \beta|\psi_{m,n}|^2 \\ \beta|\phi_{m,n}|^2 & |\psi_{m,n}|^2 \end{pmatrix} \right] \begin{pmatrix} \phi_{m,n} \\ \psi_{m,n} \end{pmatrix} = 0, \tag{7.46}$$

where β is used to denote the strength of the XPM (and equal SPMs [self-phase modulations] are assumed). In that setting, it was found by appropriately extending

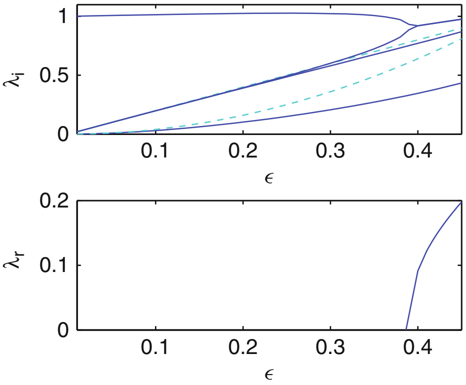

Fig. 7.10 Eigenvalues of the scalar vortex cross versus ϵ from [19]. The *top panel* shows the imaginary part of the relevant eigenvalues, while the *bottom panel* shows the real part. The *solid lines* display the numerical results, while the *dashed* ones correspond to the asymptotic approximations given in the text

the LS technique to the multicomponent setting (see [19] for details) that it is possible to compute the relevant eigenvalues as a function of β. Two leading order pairs of these eigenvalues preserve the form of the one-component problem ($\lambda = \pm 2i\epsilon$), but then there exists a pair which is intrinsically dependent on β at the leading order, namely $\lambda = \pm 2i\epsilon\sqrt{(1-\beta)/(1+\beta)}$ (which is shared by both double and hidden charge configurations). More importantly, at the next order, the eigenvalues of the $(1, 1)$ configuration *differ* from those of the $(1, -1)$ configuration. In particular, for the former we have a pair $\lambda = \pm 4i\epsilon^2$ and one which is $\lambda = \pm 4i|(1-\beta)/(1+\beta)|\epsilon^2$, while for the latter there is a double pair $\lambda = \pm 4i\sqrt{(1-\beta)/(1+\beta)}\epsilon^2$. Interestingly, these differences in eigenvalues are evident also in the numerical results illustrated in Fig. 7.11; note, in particular, the marked differences between the $(1, 1)$ and $(1, -1)$ eigenvalues, and the good agreement of both with the corresponding theoretical result for small $\epsilon < 0.1$. Along the same vein, it should be pointed out that the double charge branch $(1, 1)$ becomes unstable for $\epsilon > 0.395$, while the $(1, -1)$ branch becomes unstable only for $\epsilon > 0.495$, i.e., has a wider stability interval. We have found this to be generally true for the cases with $\beta < 1$. On the other hand, for values of $\beta > 1$, both branches are always unstable (i.e., $\forall\epsilon$). Lastly, the most delicate case is that of $\beta = 1$, whereby there is an additional homotopic symmetry between the two components, as both the transformations $\phi_{n,m} = \cos(\delta)\Phi_{n,m}$ and $\psi = \sin(\delta)\Phi_{n,m}$ (pertaining to the $(1, 1)$ solution for $\delta = \pi/4$) and $\phi_{n,m} = \cos(\delta)\Phi_{n,m}$ and $\psi = \sin(\delta)\Phi^*_{n,m}$ (pertaining to the $(1, -1)$ solution for $\delta = \pi/4$), yield a one-component equation (and δ is a free parameter). Hence, these cases need to be treated specially, as was done in [19], with the, perhaps somewhat unexpected, result that this special case leads to stability for small ϵ in the $(1, 1)$ case, while it results in *immediate* instability for the $(1, -1)$ case due to a double real eigenvalue pair $\lambda = \pm 2\sqrt{3}\epsilon^2$ (note the marked difference between this special case and the cases with $\beta < 1$).

In addition to these solutions associated with $S = 1$, it is also possible to obtain similar results for the different vortex pairs of $S = 3$, in the form of both double charge $(3, 3)$ and hidden charge $(3, -3)$ vortices, as is illustrated in Fig. 7.12 for $\epsilon = 0.25$ and $\beta = 2/3$. In this particular case, for both types of configuration,

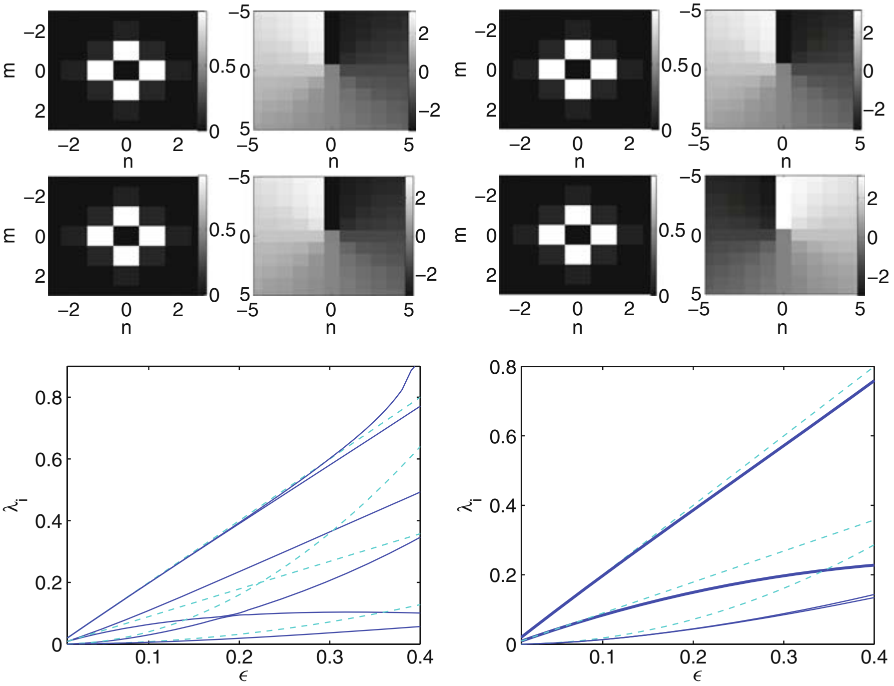

Fig. 7.11 From [19]: the contour plots of the *top two rows* show the amplitude and phase (*left* and *right panels*, respectively) of the two components (*top* and *bottom*, respectively) for a (1, 1) (*left* four subplots) and a (1, −1) (*right* four subplots) vortex configuration, in the case of $\beta = 2/3$, and $\epsilon = 0.1$. The *bottom two rows* show for the case of $\beta = 2/3$ the eigenvalues of the vector vortex cross as a function of ϵ. Left: (1, 1). *Right*: (1, −1). The *solid lines* show the numerical results, while the *dashed lines* show the asymptotic approximations. Bold curves correspond to double eigenvalues

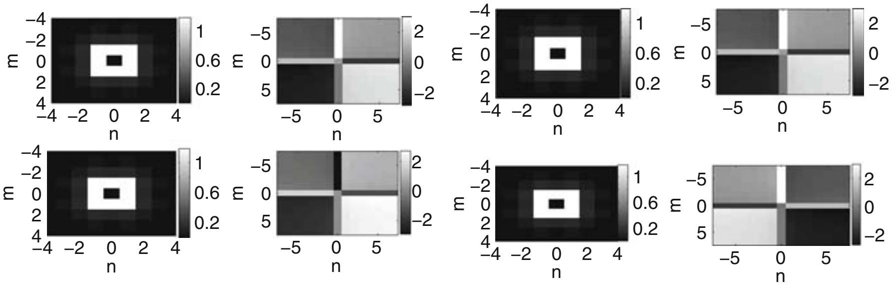

Fig. 7.12 The *left panels* show the case of a double charge with $S = 3$ (i.e., a (3, 3) two-component vortex, similarly to the *top two rows* of Fig. 7.11 above). The *right panels* illustrate the hidden charge case of a (3, −3) two-component vortex. Both are for $\epsilon = 0.25$ and $\beta = 2/3$

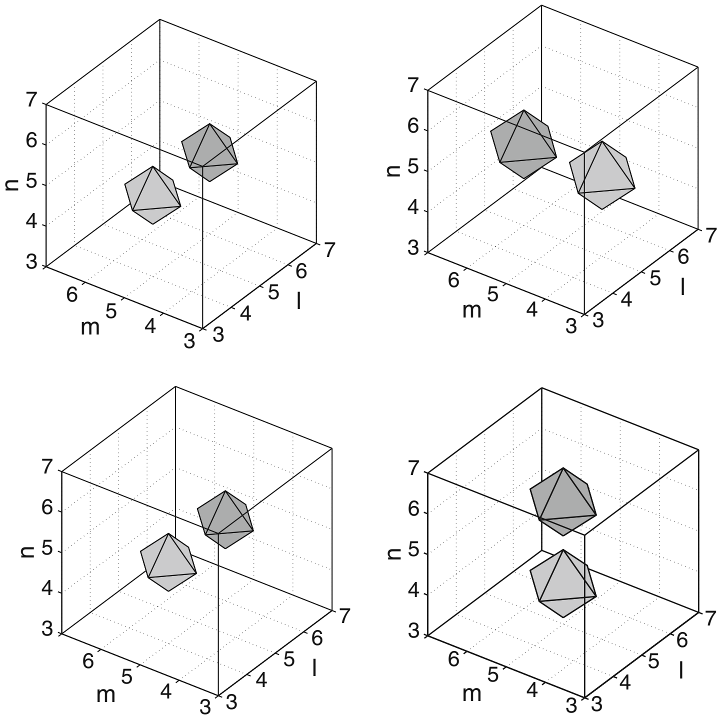

Fig. 7.13 A complex of two-component orthogonal vortices with $S = 1$ from [21] in the two-component three-dimensional system is shown for $\epsilon = 0.01$ and $\beta = 0.5$. The *top panels* correspond to the first component, while the bottom ones to the second component; the *left panels* show the respective real parts, while the right ones the corresponding imaginary parts

the instability occurs for $\epsilon \geq 0.1$; however, again the differences in the relevant eigenvalues and instability growth rates are evident. For instance, for $\epsilon = 0.4$, the growth rate of the most unstable eigenvalue for the $(3, 3)$ configuration is 0.3077, while for the $(3, -3)$ one it is 0.2097.

Finally, as an interesting example of a possibility that arises in such multicomponent systems in three spatial dimensions, we illustrate the result of Fig. 7.13, whereby a stable vortex complex has been constructed in which one component has a vortex in the (l, m) plane, while the other has a vortex in the (m, n) plane (perpendicular to the first one). Such configurations were indicated in [21] as being stable for sufficiently small ϵ, again in the case where $\beta < 1$ (while they should be expected to be unstable for $\beta > 1$).

References

1. Hudock, J., Kevrekidis, P.G., Malomed, B.A., Christodoulides, D.N.: Phys. Rev. E **67**, 056618 (2003) 153, 158, 167
2. Horne, R., Kevrekidis, P.G., Whitaker, N.: Phys. Rev. E **73**, 066601 (2006) 153, 159, 160, 162, 163, 164, 165

3. Meier, J., Hudock, J., Christodoulides, D.N., Stegeman, G., Silberberg, Y., Morandotti, R., Aitchison, J.S.: Phys. Rev. Lett. **91**, 143907 (2003) 153, 158, 159, 160, 162, 163
4. Jin, G.-R., Kim, C.-K., Nahm, K.: Phys. Rev. A **72**, 045601 (2005) 153
5. Alfimov, G.L., Kevrekidis, P.G., Konotop, V.V., Salerno, M.: Phys. Rev. E **66**, 046608 (2002) 153
6. Ballagh, R.J., Burnett, K., Scott, T.F.: Phys. Rev. Lett. **78**, 1607 (1997) 153
7. Deconinck, B., Kevrekidis, P.G., Nistazakis, H.E., Frantzeskakis, D.J.: Phys. Rev. A **70**, 063605 (2004) 153
8. Ohberg, P., Stenholm, S.: Phys. Rev. A **59**, 3890 (1999) 153
9. Williams, J., Walser, R., Cooper, J., Cornell, E., Holland, M.: Phys. Rev. A **59**, R31 (1999) 153
10. Herring, G., Kevrekidis, P.G., Malomed, B.A., Carretero-González, R., Frantzeskakis, D.J.: Phys. Rev. E **76**, 066606 (2007) 154, 156, 157, 158, 159
11. Flach, S., Kladko, K., MacKay, R.S.: Phys. Rev. Lett. **78**, 1207 (1997) 158
12. Weinstein, M.I.: Nonlinearity **12**, 673 (1999) 158
13. Kastner, M.: Phys. Rev. Lett. **93**, 150601 (2004) 158
14. Kevrekidis, P.G., Rasmussen, K.Ø., Bishop, A.R.: Phys. Rev. E **61**, 2006 (2000) 158
15. Lederer, F., Darmanyan, S., Kobyakov, A.: In: Spatial Optical Solitons. Trillo, S., Torruellas, W.E. (eds.) Springer-Verlag, New York, (2001) 158
16. Darmanyan, S., Kobyakov, A., Schmidt, E., Lederer, F.: Phys. Rev. E **57**, 3520 (1998) 158
17. Kevrekidis, P.G., Nistazakis, H.E., Frantzeskakis, D.J., Malomed, B.A., Carretero-González, R.: Eur. Phys. J. D **28**, 181 (2004) 158
18. Ablowitz, M.J., Musslimani, Z.H.: Phys. Rev. E **65**, 056618 (2002) 158
19. Kevrekidis, P.G., Pelinovsky, D.E.: Proc. R. Soc. A **462**, 2671 (2006) 158, 167, 168, 169
20. Kevrekidis, P.G., Malomed, B.A., Frantzeskakis, D.J., Carretero-González, R.: In: Focus on Soliton Research. Chen, L.V. (ed.) pp. 139–166. Nova Science Publishers, New York, (2006) 158, 167
21. Kevrekidis, P.G., Malomed, B.A., Frantzeskakis, D.J., Carretero-González, R.: Phys. Rev. Lett. **93**, 080403 (2004) 158, 167, 170
22. Meier, J., Hudock, J., Christodoulides, D.N., Stegeman, G.I., Yang, H.Y., Salamo, G., Morandotti, R., Aitchison, J.S., Silberberg, Y.: J. Opt. Soc. Am. B **22**, 1432 (2005) 158
23. Vicencio, R.A., Molina, M.I., Kivshar, Yu.S.: Opt. Lett. **29**, 2905 (2004) 159
24. Vicencio, R.A., Molina, M.I., Kivshar, Yu.S.: Phys. Rev. E **71**, 056613 (2005) 159
25. Rapti, Z., Trombettoni, A., Kevrekidis, P.G., Frantzeskakis, D.J., Malomed, B.A., Bishop, A.R.: Phys. Lett. A **330**, 95 (2004) 159
26. Meier, J., Stegeman, G.I., Christodoulides, D.N., Silberberg, Y., Morandotti, R., Yang, H., Salamo, G., Sorel, M., Aitchison, J.S.: Phys. Rev. Lett. **92**, 163902 (2004) 162
27. Desyatnikov, A.S., Mihalache, D., Mazilu, D., Malomed, B.A., Denz, C., Lederer, F.: Phys. Rev. E **71**, 026615 (2005) 167
28. Ye, F., Wang, J., Dong, L., Li, Y.P.: Opt. Commun. **230**, 219 (2004) 167
29. Malomed, B.A., Kevrekidis, P.G.: Phys. Rev. E **64**, 026601 (2001) 167